The International Journal of Advanced Manufacturing Technology (2023) 126:1159–1173
https://doi.org/10.1007/s00170-023-11153-2

ORIGINAL ARTICLE

Information-rich quality controls prediction model based on non-destructive analysis for porosity determination of AISI H13 produced by electron beam melting

Cristian Ghibaudo[1] · **Giacomo Maculotti**[2] · **Federico Gobber**[1] · **Abdollah Saboori**[2] · **Maurizio Galetto**[2] · **Sara Biamino**[1] · **Daniele Ugues**[1]

Received: 10 October 2022 / Accepted: 23 February 2023 / Published online: 8 March 2023

Abstract

The number of materials processed via additive manufacturing (AM) technologies has rapidly increased over the past decade. As of these emerging technologies, electron beam powder bed fusion (EB-PBF) process is becoming an enabling technology to manufacture complex-shaped components made of thermal-cracking sensitive materials, such as AISI H13 hot-work tool steel. In this process, a proper combination of process parameters should be employed to produce dense parts. Therefore, one of the first steps in the EB-PBF part production is to perform the process parameter optimization procedure. However, the conventional procedure that includes the image analysis of the cross-section of several as-built samples is time-consuming and costly. Hence, a new model is introduced in this work to find the best combination of EB-PBF process parameters concisely and cost-effectively. A correlation between the surface topography, the internal porosity, and the process parameters is established. The correlation between the internal porosity and the melting process parameters has been described by a high robust model ($R^2_{\mathrm{adj}}=0.91$) as well as the correlation of topography parameters and melting process parameters ($R^2_{\mathrm{adj}}=0.77$–0.96). Finally, a robust and information-rich prediction model for evaluating the internal porosity is proposed ($R^2_{\mathrm{adj}}=0.95$) based on in situ surface topography characterization and process parameters. The information-rich prediction model allows obtaining more robust and representative model, yielding an improvement of about 4% with respect to the process parameter-based model. The model is experimentally validated showing adequate performances, with a RMSE of 2% on the predicted porosity. This result can support process and quality control designers in optimizing resource usage towards zero-defect manufacturing by reducing scraps and waste from destructive quality controls and reworks.

Keywords Electron beam melting · Electron beam powder bed fusion · H13 steel · Additive manufacturing · Porosity · Non-destructive quality control · Surface topography

Highlights

- A model is created correlating process parameters and internal porosity.
- Correlation between internal porosity and surface topography is demonstrated.
- Accordingly, an information-rich porosity prediction model is created.
- The method to predict porosity by in situ information is applied to H13 by EBM.
- The information-rich prediction model improves representativeness of 4%.

✉ Giacomo Maculotti
giacomo.maculotti@polito.it

[1] Department of Applied Science and Technology, Politecnico di Torino, Corso duca Degli Abruzzi 24, 10129 Torino, Italy

[2] Department of Management and Production Engineering, Politecnico di Torino, Corso duca Degli Abruzzi 24, 10129 Torino, Italy

1 Introduction

Additive manufacturing (AM) techniques are improving fast, thanks to the increasingly available materials and the quality of the final products. Among the various AM techniques, electron beam powder bed fusion (EB-PBF), also known as electron beam melting (EBM), is a powder bed fusion additive manufacturing technique that selectively melts layer by layer the powder bed using an electron beam in order to build the final components (see Fig. 1) [1]. EB-PBF produces metallic components with a density above 99.5% using optimized process parameters [2–6]. The detailed steps of the process can be found in the work of Murr et al. [1]. The two main characteristics of EB-PBF are the vacuum environment and the preheating temperature (up to 1100 °C). The first limits the interstitial element content in the final

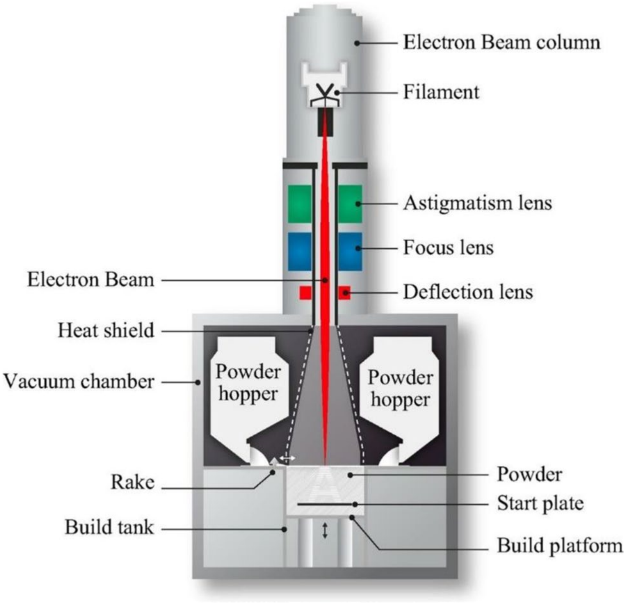

Fig. 1 Scheme of main element of electron beam melting (EBM) process. During the process a layer of powder is laid on the build plate by the hoppers and levelled by the rake. The EB generated by the column, focused and directed by the lenses locally melt the powder to build the cross-section. The build platform is moved downward, and the process repeats to achieve the layer-by-layer manufacturing

components [6, 7]. The second is a crucial characteristic for the processability of sensitive materials prone to thermal cracking [4, 8–12] since it enables the reduction of residual stresses in the final components [13]. These primary advantages drive the increasing interest in the EB-PBF process.

An example of crack-sensitive material is the AISI H13 steel. This material is widely used to produce die-casting, and extrusion dies for hot working applications[14, 15]. Thanks to its microstructure consisting of martensite and Cr, Mo, and V-based secondary carbides, AISI H13 provides high thermal stability and hardness up to 550–600 C [16]. Cormier et al. [5] firstly investigated the production of AISI H13 by the EB-PBF process. More recently, literature addressed the study of the microstructures and the mechanical properties of AISI H13 samples processed by the EB-PBF process [17, 18]. The EB-PBF production of AISI H13 components allows the possibility to produce novel optimized designs and conformal dies to increase the components' productivity and lifetime. These concepts were preliminarily studied by Rännar et al. [14] and Gibbons et al. [15].

AM is well known to increase material efficiency, although it is associated with high cost. It becomes competitively convenient with respect to conventional manufacturing processes for highly customized products, which characterizes the customer demand. Despite the improved material consumption, on the route towards sustainability, the optimization process is still critical. In fact, process parameter optimization to reduce internal and external defects to comply with technical and functional specifications of geometry, material structure, and mechanical properties is still affected by a consistent amount of scraps and waste. Moreover, even when the process is optimized, quality controls for internal defects, i.e., porosity, are most typically destructive or expensive.

The most diffused procedure to identify and quantify the internal defects consists of time-consuming destructive (D) methods, e.g., the cross-sectioning of the samples and subsequent optical microscope image analysis [18–20]. On the other hand, non-destructive (ND) testing methods, and among them Archimedes [21], gas pycnometers [20], and ultrasonic-based methods [22], can be very fast compared to the traditional destructive methods, but present some limitations in the defect's accurate identification and, consequently, their quantification [23]. The most advanced ND technique is X-ray computer tomography, which gives in-depth information about internal defects [23–25]. Nonetheless, the high capital cost of investment and long analysis time of the computer tomography limits its application in the defect analysis during the optimization process [26, 27].

Furthermore, all the above mentioned inspection techniques require post-processing of specimens and are thus off-line [23, 28]. It is clear that during process optimization, off-line quality controls are inevitable. However, on the route towards sustainability, zero waste, and zero defects, once the process has been optimized, destructive control shall be minimized, if not avoided entirely. This can be achieved by developing predictive models based on in-line and in situ quality controls that can source information while the process is still ongoing and give valuable feedback for on-line improvements. The equipment for some of these in situ techniques for powder bed fusion is commercially available and can give information on the internal defects during the process [29]. Such predictive models relate process parameters and other available information by in situ inspection techniques to defects and often can be obtained by advanced statistical techniques while relying on big data. Indeed, destructive quality controls are necessary to validate those predictive models. Such a framework allows the creation of adequate and information-rich non-destructive quality controls, whose advantages are definitive and twofold [28, 29]: real-time process control and scrap reduction [30–33]. It is worth remarking that the informativeness of destructive or expensive inspection techniques is paramount when studying process parameters windows for innovative materials and setting up the processes. However, during the process optimization and production, they lead to unnecessary costs if robust alternative routes of quality inspection are available.

In situ inspection methods rely on different signals, ranging from raw process parameters and embedded sensors (level-0) to progressively refined and high-resolution measurement methods [29].

Surface characteristics are among the several aspects that in situ inspection techniques can tackle. In fact, due to the layer-by-layer nature of the process, the final surface resembles the population of the internal defects with a certain confidence. This correspondence can be found in the literature [21, 34, 35], where a qualitative distinction between the different surfaces has been correlated with the internal porosity. However, design specification and quality control require quantitative characterization [36, 37], achievable by evaluating surface topography parameters [38, 39]. Such quantitative characterization requires exploiting surface topography measuring instruments. Several alternatives are available on the market, e.g., coherence scanning interferometry (CSI), focus variation, and confocal microscopy [40]. However, they differ in metrological performances in the AM field and the suitability for in-line quality controls. Literature reports that the CSI is the most accurate [40], but its working principle hinders application in harsh environments such as the AM building chamber. Therefore, innovative systems based on focus variation [41] and fringe projection are developed for in-line control [42], and they are reported as level-1 in situ inspection methods [29].

The study of a potentially new EB-PBF-processable material involves optimizing the melting process parameters. This could be time- and cost-consuming due to the many combinations necessary to explore the possible process window. Melting optimization aims to achieve targeted geometrical design characteristics and minimize internal defects (if their complete avoidance is impossible) while maximizing productivity. Several studies reported the influence of process parameters on the final quality of the component for various materials [7, 12, 29, 43]. Melting parameters and the powder's quality influence the final component's relative density and hence affect a wide range of mechanical properties [7, 12, 28]. Amongst the melting parameters, the melting strategy, the beam power, which depends on the voltage and the beam current, the scanning speed, and the line offset, are the most relevant. In addition, these process parameters are the key parameters that define the type and contents of the defects, e.g., lack of fusion and gas pores, as well as the as-built microstructure of the components [7, 44–46].

Generally, a design of experiment (DoE) is resorted to investigating the effect of melting parameters on the defects generated during the EB-PBF process. The DoE can be used to select statistically significant factors, i.e., parameters and their interactions, to be included in statistical models to relate process parameters, signals from in situ inspection, and quality characteristics of the components. These models can then be exploited for process optimization to find a proper process window where the parts can be produced with minimum internal defects. For example, Guo et al. [47] showed that the relative density of Ti-6Al-4 V specimens produced through the EB-PBF process is inversely proportional to scanning speed and directly proportional to the beam current. Additionally, they showed the qualitative dependence of the top surface on the internal porosity [47]. Although these studies have paved the way for understanding mechanisms, they all provide qualitative relationships between process parameters, microscale geometrical properties, and internal defects of the EB-PBF parts.

This work aims to establish an information-rich prediction model of the internal porosity from surface topography and input process parameters.

In this work, a mathematical model is proposed to correlate the topographical surface features (level-1 inspection) and the process parameters (level-0 inspection). Similarly, a mathematical model correlating the internal porosity and process parameters is presented. Finally, these models are exploited to build the information-rich predictive model. The development of this model is essential for zero-defect manufacturing and the creation of a digital twin of the processes to achieve complete real-time control of the process.

2 Materials and methods

2.1 Sample production

In this work, a gas atomized AISI H13 powder with a particle size range from 40 to 150 µm ($d_{10}=45$, $d_{50}=57$ µm, $d_{90}=70$ µm) supplied by Sandvik was used as the feedstock material. The chemical composition of the powder is reported in Table 1. The particles are mainly spherical, with a high presence of satellites; in Fig. 2, an example of the powder is reported.

The samples were produced using an ARCAM A2X EB-PBF machine. The cubic AISI H13 specimens with a dimension of $30\times30\times30$ mm^3 were built on a stainless-steel start plate. The preheating temperature was kept constant and set at 700 °C for all the specimens produced in this work. Two levels of layer thickness (t) (50 µm and 90 µm) and the snake-like scan pattern with 90° rotation per layer were used in the sample's production. In the DoE, different combinations of process parameters were selected to study their individual influence and relative interactions. The considered process parameters were the focus offset (FO), the beam speed (v), the beam current (I), and line offset (LO). The experimental plan considered the five factors mentioned above, i.e., t, I, v, LO, and FO, which were varied on 2, 2, 10, 3, and 4 levels, respectively. The levels for each factor were chosen based on the literature [5, 18]. According to industrial practices and relying upon authors' experience [2, 48, 49], some conditions

Table 1 Nominal chemical composition of AISI H13 powder, when available, the measured values are indicated by *

Alloy	Fe (wt.%)	C (wt.%)	Cr (wt.%)	Ni (wt.%)	Mo (wt.%)	Si (wt.%)	Mn (wt.%)	V (wt.%)	O (wt.%)	N (wt.%)
AISI H13	Bal	0.35*	4.75–5.50	0.3	1.10–1.75	0.8–1.2	0.2–0.5	0.8–1.2	0.19*	0.055*

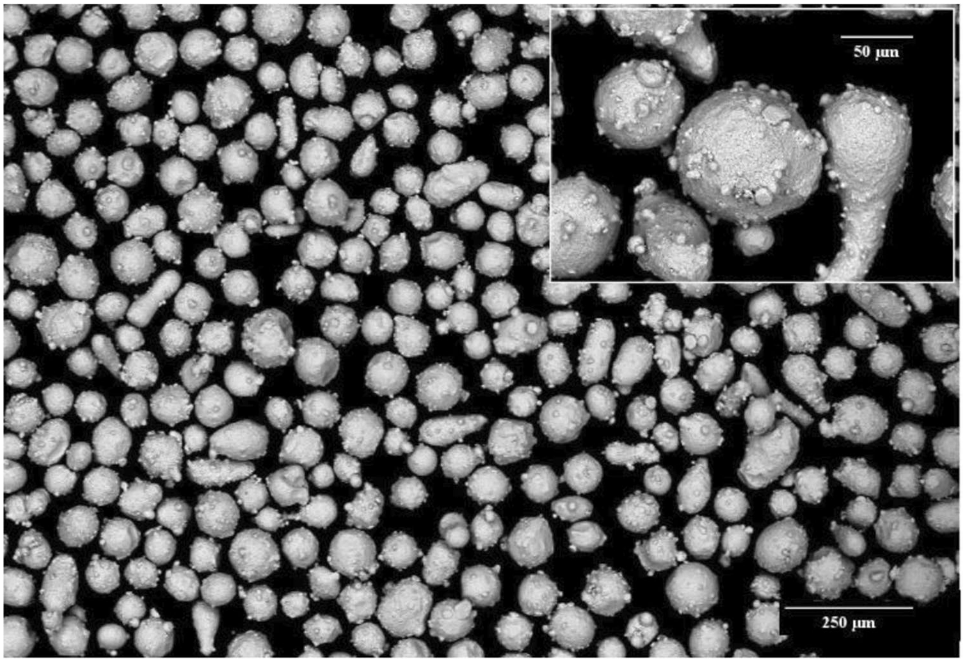

Fig. 2 AISI H13 powder micrographs obtained via SEM

were removed or modified during the building process since they already showed a high presence of defects or could be harmful to the successful process completion. Some replications were introduced randomly to extend the number of data and improve the dataset robustness. This approach resulted in an unbalanced DoE, as reported in Table A1 in the Appendix, with 52 investigated conditions.

2.2 Top surface topographical analysis

The top surface topography was measured by CSI. NewView 9000 by Zygo and characterized according to the literature [38, 39] following the ISO 25178–2:2018 standard. The measurement was set up considering literature best practices [50]: a Michelson × 5.5 objective lens with a numerical aperture of 0.15 was adopted, applying a 0.5 × digital zoom and resulting in a field of view (FOV) of 3.15 × 3.15 mm^2 with a lateral sampling resolution of 3.15 μm/pixel. Stitching of 4 × 3 FOVs resulted in an investigated area of at least 10 × 8 mm^2. In addition, signal oversampling was applied [50] to reduce noise and non-measured points due to high surface roughness, typical of AM topographies. As mentioned in the introduction, CSI is the most accurate and precise measurement method, but the harsh build chamber environment hinders its application as an in situ measurement technique. However, literature has shown that other surface topography native measurement methods that can be mounted in the build chamber, e.g., focus variation and fringe projection systems, yield characterization results compatible with CSI measurements [41, 42, 51].

The characterization includes a first correction of spikes and non-measured points [52, 53]. Then, the measured surface was filtered by applying a robust gaussian S-filter, i.e., a high-pass filter in the wavelength domain, to suppress measurement noise with a nesting index of 10 μm [53, 54]. Then, the F-operator removes the form by suppressing the least-square fitted plane. Subsequently, according to the state-of-the-art prescription [38, 39, 55], the waviness surface must be isolated. This is performed by applying a robust gaussian L-filter [53]. The nesting index is chosen as the topography's smooth-to-rough crossover (SRC). This particular choice allows tailoring the separation of the waviness surface and the SL-Surface to the topography in analysis by identifying the separation scale, i.e., the wavelength, between the two surface topography content by scale-sensitive fractal-analysis [53, 56]. The waviness surface is then characterized by evaluating the S_a, S_q, and S_{dq} area field parameters [53]. This characterization step is relevant because the waviness surface can bear a low-scale manufacturing signature, e.g., swollen surfaces [21]. The residual of the waviness removal, i.e., the SL-Surface, is then exploited to perform a feature-based characterization that describes the globules and topographical pores on the surface. Globules and topographical pores are surface defects due to several causes, e.g., attached particles, Marangoni flow, internal cavities, and porosities causing surface recesses[21, 34, 38]. They can be identified by watershed segmentation, which in this work it is applied with a wolf-pruning at three times the standard deviation of the surface topography heights [38]. The overall volume characterizes globules and pores (V_g and V_p) and the area percentage to the whole surface ($A_{\%g}$ and $A_{\%p}$ [38, 39]). Once the features are identified, they are removed and the *actual* roughness surface, i.e. the *actual* SL-Surface, is then characterized by evaluating S_a, S_q, S_{dq}, S_{sk}, and S_{ku}. Surface topography analysis is performed by the state-of-the-art software Mountains Lab v8.0.

2.3 Internal porosity analysis

All the as-built specimens were cut parallel to the building direction and ground with SiC paper, up to 2500 grit. Then, all the samples were polished with diamond paste, down to 1 μm, to obtain a mirror-like surface. A Leica DMI 5000 M metallographic optical microscope (OM) was used to collect 20 images at 50× per specimen. The micrographs were analyzed using ImageJ software, and the internal porosity content was determined following the procedure described in the ASTM E2109-01 standard [57]. Per each of the 52 examined specimens, 20 porosity data (percentage), $p_{ij}, i = \{1, \dots, i = 52\} \subset \mathbb{N}$ and $j = \{1, \dots, J = 20\} \subset \mathbb{N}$, were collected per specimen. The resulting average porosity percentage for each condition, $\overline{p}_i = \frac{\sum_{j=1}^{J} p_{ij}}{J}$, was obtained prior the elimination of potential outliers, identified by the modified inter-quartile range (IQR) outlier method [58].

2.4 Statistical analysis

The unbalanced DoE outcomes are analyzed employing the Generalized Linear Model (GLM) technique to identify process parameters and their interactions that statistically influence in a significative way the surface topographical parameters $S_\blacksquare$ and the porosity p (let $S_\blacksquare$ be any considered surface topography parameters introduced in Sect. 2.1 [59]). GLM is a supervised machine learning technique that allows drawing statistical models between a set of predictors, i.e., input variables, and some outputs whose probability distribution can be approximated by a density belonging to the exponential family and, in the case at hand, outputs are assumed to be normally distributed. The model is a linear combination of the predictors, passing through a non-linear function [60]. In literature, the melting process parameters are generally expressed as line energy ($LE = (V \cdot I)/v$) or area energy ($AE = LE/LO$) [61], where V is the voltage of the electron beam source, which is set to 60 kV in the Arcam A2X machine. Therefore, the LE and AE values have been calculated and introduced in the regression model to cater for a possible non-linear combination of the DOE factors. Another relevant process parameter is the speed function (SF). It is generally used during production with a positive value correlating the I and v with a black-box function developed by Arcam GE. This operative melting parameter aims to homogenize the heat distribution on the overall melting area of the specimen. However, it is preferable to use negative SF values that correspond to a linear ratio of v and I during the optimization step, i.e., $SF = -v/I$, allowing manual setup. The GLM estimates the coefficients of the models, i.e., of the linear combination of the input variables, by the least square method, i.e., maximizing the log-likelihood estimation [59, 60]. Accordingly, GLM allows estimating the models $h_\blacksquare$ and f:

$$S_\blacksquare = h_\blacksquare(\boldsymbol{x}) \tag{1}$$

$$p = f(\boldsymbol{x}) \tag{2}$$

where $h_\blacksquare$ is the generic model for any $S_\blacksquare$, and $\boldsymbol{x} = \{t, I, v, FO, LO, LE, AE, SF\}$ is the input variable array. GLM is typically exploited in literature to quantitatively investigate the effect of process parameters on some quantity of interests [62, 63].

Linear polynomial models of the third order with second-order interactions are considered. However, not all the terms may be statistically significant. In this work, the statistical significance of the terms is set at the conventional confidence level of 95%, i.e., terms associated with a p-value greater than 5% are not statistically significant. Analysis of variance (ANOVA) is typically resorted to properly assess the statistical significance of the estimated parameters, accounting for the degrees of freedom of the estimation and the error, i.e., the fitting residuals. Consequently, the presence of statistically non-significant terms worsens the model's predictive performance, for it reduces the degrees of freedom available to estimate the error. Therefore, variable reduction is a non-trivial issue primarily investigated in the literature. In this work, the variable reduction is tackled by the stepwise method, which obtains a model solely consisting of significant terms by adding and removing predictors in a sequence of steps according to selected alpha-to-enter and alpha-to-remove thresholds [64–66], here both conventionally set at 15% [64].

The application of GLM requires the verification of the base hypothesis, i.e., that the response variable is normally distributed and that the estimated model does not ignore systematic trends in the data, i.e., that the residuals are normally distributed. Normality tests are performed graphically by normal probability plot (NPP) and quantitatively by Anderson–Darling test, at a confidence level of 95%. The goodness of fit is evaluated by testing the normality of the residuals and by computing the R^2_{adj} [59]. Here, the R^2_{adj} is preferred to R^2 to compare different models, because it normalises the latter with a factor proportional to the number of terms in the model, so that if two models are equally representative, but one requires more terms, it is associated with a smaller R^2_{adj}.

2.5 Information-rich prediction model

This work aims at establishing an information-rich prediction model of internal defectivity, intended as porosity, as a function of process parameters while also exploiting the characterization of surface topography to enrich informativeness and increase robustness. Thus, it tackles the estimation of the function f_{i-r}:

$$p = f_{i-r}(\boldsymbol{x}, S_\blacksquare) \tag{3}$$

The first step toward the model creation is analyzing the correlation between the porosity and surface topography parameters. This is essential to establish which parameters are correlated to and physically influenced by porosity. This step is conceptually essential for the creation of the information-rich prediction model. Only parameters that are correlated to porosity can be exploited to predict it. Correlation analysis is performed qualitatively through scatter plot and quantitatively by GLM, with variable selection performed by stepwise method. GLM is applied, considering as predictors the $S_{\blacksquare}$ whose scatter plots suggest a possible correlation; this choice allows considering the most appropriate terms as regressors of Eq. 3. It is worth remarking here that, although the physical relation is $S_{\blacksquare} = S_{\blacksquare}(p)$ if a correlation is present, the application at hand requires reversing that information. In fact, during the production, process parameters are set and controlled, and the resulting surface topography parameters can be inspected. These are the available input information exploited as regressors to estimate the model $f_{i\text{-}r}$.

The functional form and related parameters of the information-rich prediction model of Eq. 3 is estimated by stepwise GLM. The goodness of fit is evaluated by testing the normality of the residuals and reporting the R^2_{adj}.

The analyzed process window is sufficiently far from the origin of the hyperspace described by the regressors. Therefore, evaluating the evaluated models' intercept can be carried out merely based on mathematical discussions, i.e., to maximize the goodness of fit. From the process physics perspective, the discussion of the evaluated models' behaviour in the origin neighbourhood is negligible.

The model is trained on the available dataset (see Appendix), excluding replicated conditions. The replications will be exploited to validate the model, by evaluating the prediction interval and performing hypothesis test to assess statistical compatibility of the predicted value with respect to the experimental measurement.

3 Results and discussion

Table 2 summarizes the measurement unit used in this work and to which the estimated parameters of the model refer.

Table 3 reports the investigated process window regarding the considered factors' minimum and maximum levels.

3.1 Top surface analysis

Figure 3 shows some representative results of the top surface topography measurements according to the methodology described earlier. According to the literature, several types of topographies can be distinguished, characterized by more or less severe geometrical errors, large topographical features, and deviation from nominal geometry. These can be classified into clean, wavy, and orange-peel topographies, which might also present some additional localized features, e.g., globules or pores [21, 34, 38].

The set of fields and feature surface parameters are evaluated following the previous methodology.

Stepwise, GLM is applied to the *SRC*, the field parameters evaluated on the waviness surface, i.e., S_a, S_q, and S_{dq}, and on the feature parameters evaluated on the SL-Surface, i.e. V_g, V_p, $A_{\%g}$ and $A_{\%p}$. Table 4 reports the R^2_{adj} and the mathematical models correlating the surface topography parameters to the process parameters. Only statistically significant interactions and parameters, at a confidence level of 95%, are present in the GLM model, thanks to the application of the stepwise variable reduction. Residuals of the models did not show any trend, and the Anderson–Darling normality test could not reject the null hypothesis of normality with a risk of error of 5%.

The resulting different surface regression models consider the combination of the melting process parameters. In particular, S_a and S_q regression model terms are the same. They indicate an interaction between the *I* and *t* since the melt pool depth is strongly dependent on the beam current [67], while FO, which influences the melt pool width, interacts with the *LO* of subsequent line scan. The S_{dq} regression model shows the correlation between the surface waviness and melt pool geometry since the *FO*, *SF*, and *I* are the main process parameters defining the melt pool characteristics.

The identification and the removal by segmentation of the topographical features allow the characterization of the *actual* SL-Surface in terms of S_a, S_q, S_{dq}, S_{sk}, and S_{ku}. Because a wide range of processing conditions is addressed, some of which are far from optimal, a few topographies may result dominated by features, e.g., orange peel topographies, that hinder the evaluation

Table 3 Factors considered in the unbalanced DOE with maximum and minimum levels

Factor	Min. level	Max. level
LO/mm	0.2	0.3
FO/mA	15	35
SF/mm/(mA·s)	−400	−46.7
I/mA	8	15
t/mm	0.05	0.09

Table 2 Measurement unit of considered process parameters and quality control variables. Estimated statistical model parameters are homogeneous with these. "-" indicates adimensional values, "%" percentage in the 0–100 range

Parameter	Lo	FO	SF	I	LE	AE	*t*	SRC	*p*
Unit	mm	mA	mm/(mA·s)	mA	J/mm	J/mm^2	mm	µm	%
Parameter	S_a	S_q	S_{dq}	S_{sk}	S_{ku}	V_g	V_p	$A_{\%g}$	$A_{\%p}$
Unit	µm	µm	-	-	-	mm^3	mm^3	%	%

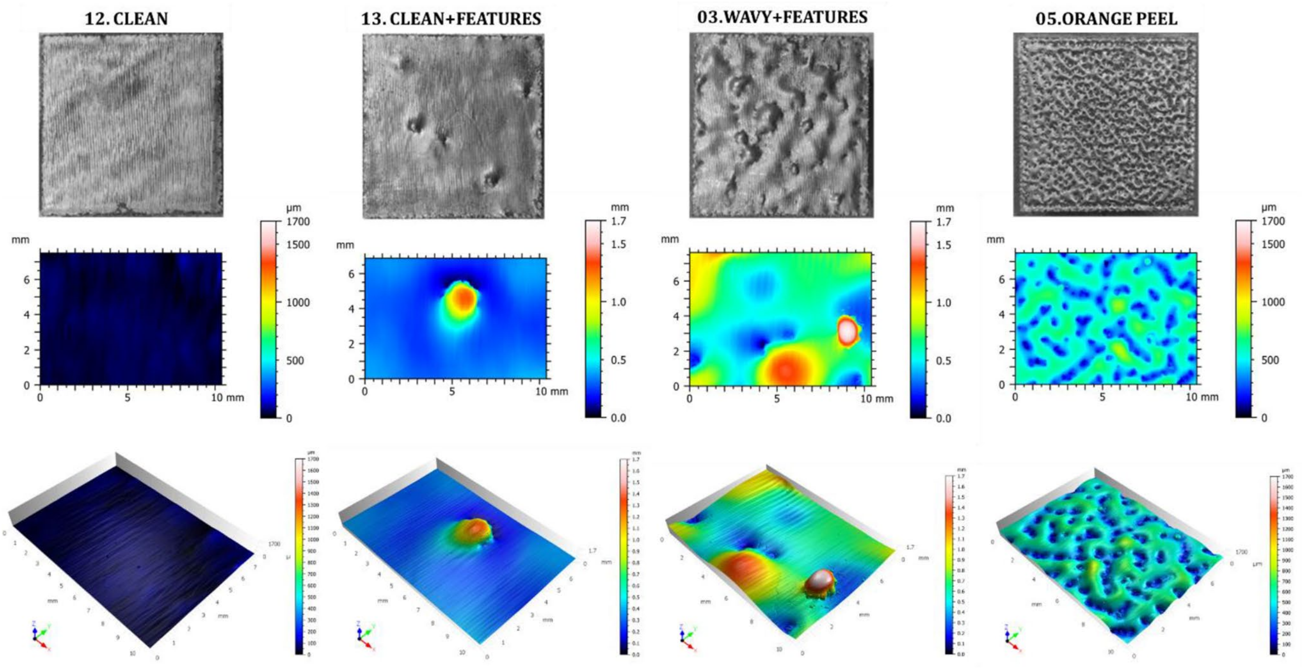

Fig. 3 Visual inspection of top surface topography at different scales. Top row: images by an optical camera at low magnification, central and bottom row, pseudo colour height maps measured by the CSI. Height scales are different to appreciate details of topographical features

of characterization parameters. Stepwise GLM modelling of the parameters is performed to investigate the correlation and the dependence of the actual SL-Surface area field parameters. Table 5 reports the results of such analysis. The ANOVA analysis to test the significance of the terms included in the models showed the statistical significance with *p*-values smaller than 5% for any terms of any model reported in both Table 4 and Table 5. The robustness and representativeness of all the models benefitted from constraining to zero the related intercept.

The results show that S_a and S_q are correlated to process parameters consistently to the common practice. However, the more robust modelling is obtained for the S_{dq} parameter. This is the average height gradient of the surface, and it describes how fast the surface slopes vary. Very low S_{dq} characterizes smoother surfaces, while rougher surfaces, rich in hills and dales, by higher values. Moreover, EB-PBF surfaces of not optimized process parameters are rich in topographical pores [38, 39]. Therefore, for AM native surfaces, it is quite an effective parameter to describe the quality of the process, although it is scarcely adopted [52]. Complementary information to S_{dq} is S_{ku} which indicates the surface's degree and amount of spikiness, i.e., how many and how sharp the positive features are. Consistently, it is strongly correlated to process parameters. The actual SL-Surface parameters shown in Table 4 depend mainly on the *I*, *FO*, and *t*, suggesting that the more significant effect on the surface parameters is induced by the electron beam diameter and the melt pool depth, and, therefore, the ability to melt multiple layers of the thickness *t*. The results obtained and shown in former tables provide quantitative evidence in relating these surface topography parameters to process variables, supporting former qualitative analysis in the literature and indicating valuable indications to process and components designers to assess the product quality.

Table 4 Results of the stepwise GLM modelling of the dependence of waviness areal field parameters and the complete SL-Surface feature parameters. Results related to V_g and $A_{\%g}$ are not shown as R^2_{adj} is smaller than 0.65, indicating a lack of representativeness and correlation of the models

Parameter	R^2_{adj}	Stepwise GLM model $S_\bullet = h_\bullet(x)$
SRC	0.77	$SRC = 7118 \bullet LO + 246.6 \bullet I + 0.355 \bullet FO \bullet SF - 1496 \bullet LE^3$
S_a	0.87	$S_a = 113.3 \bullet t \bullet I - 7.94 \bullet FO \bullet LO - 0.2174 \bullet SF \bullet AE$
S_q	0.87	$S_q = 137.3 \bullet t \bullet I - 9.62 \bullet FO \bullet LO - 0.2683 \bullet SF \bullet AE$
S_{dq}	0.91	$S_{dq} = -4.4 \times 10^{-5} \bullet FO \bullet SF + 7.33 \times 10^{-3} \bullet SF \bullet LO - 1.69 \times 10^{-4} \bullet SF \bullet I$
V_p	0.72	$V_p = -1.05 \times 10^{-4} \bullet SF^2 - 5.42 \times 10^{-3} \bullet SF \bullet I - 0.473 \bullet LE \bullet AE$
$A_{\%p}$	0.92	$A_{\%p} = 301 \bullet t - 1.73 \times 10^{-2} \bullet SF \bullet FO + 2 \times 10^{-6} \bullet SF^3$

3.2 Internal porosity analysis

The quantification of the porosity is performed through the image analysis method on 20 random images per specimen. The overall porosity is calculated and reported as an average value for each sample. From the OM cross-section of the samples, which are shown in Fig. 4, it is possible to distinguish different groups of samples: (i) large and vertical lack of fusion (Fig. 4 sample 05), (ii) random and horizontal lack of fusion (Fig. 4 sample 03), and (iii) no internal porosity or only meagre amounts of spherical pores (Fig. 4 samples 12 and 13 respectively). Furthermore, depending on the combination of the process parameters, it is possible to observe all the intermediate classes.

Analyzing the normal probability plot of the investigated specimens and performing the Anderson–Darling test, almost all samples do not follow a normal distribution at a 95% confidence level. The analyzed data are percentages, which are positively bounded and, in the case at hand, should feature a mode in the neighbourhood of zero. Accordingly, a possible better distribution fit is the lognormal distribution. Therefore, the Box-Cox transformation with λ parameter equal to 0, i.e., a natural logarithm, was applied to the measured values, and the transformed data were tested for normality. Only 4 cases of systematic deviation from normality were observed in the transformed data. In particular, the NPPs from the specimens whose porosity shows a systematic deviation from lognormality suggest a possible bimodal distribution. The analysis at the OM, see Fig. 5, corroborates this hypothesis, showing that these specimens present two well-defined and separated regions: areas with high porosity content and areas with shallow content of defects. Conversely, the specimen characterized by a lognormal porosity distribution presented, at OM analysis, homogeneously distributed defects or a complete absence of significant defects, as shown in Fig. 5 (samples 5 and 12).

Table 5 Results of the stepwise GLM modelling of the dependence of the *actual* SL-Surface, i.e., after removing features and area field parameters. Results related to S_{sk} are not shown as R^2_{adj} is smaller than 0.65, indicating a lack of representativeness of the model and correlation

Parameter	R^2_{adj}	Stepwise GLM model $S_{\bullet} = h_{\bullet}(\boldsymbol{x})$
S_a	*0.77*	$S_a = 10669 \bullet t - 1.613 \bullet FO - 59.1 \bullet I$
S_q	*0.77*	$S_q = 12812 \bullet t - 1.923 \bullet FO - 71 \bullet I$
S_{dq}	*0.85*	$S_{dq} = 155.5 \bullet t - 0.02257 \bullet FO - 0.856 \bullet I$
S_{ku}	*0.96*	$S_{ku} = 0.0929 \bullet FO + 8.05 \bullet LO - 0.1899 \bullet I$

Accordingly, to comply with GLM hypotheses, these specimens characterized by a bimodal porosity distribution were excluded from the following computation. However, the high number of remaining conditions (48) against the excluded ones (4) ensures a representative model's definition. The model relating internal porosity and process parameters was obtained via GLM, provided the application of the Box-Cox with $\lambda = 0$ transformation, and resulted in:

$$\begin{aligned} ln(p) =& 0.972 \bullet FO - 0.000132 \bullet SF^2 + 0.002650 \cdot FO \cdot SF \\ & - 1.38 \cdot FO \bullet LE + +2.007 \cdot LO \cdot I + 0.00431 \cdot I \cdot SF \\ & + 10.28 \cdot LE^3 + 0.0333 \cdot AE^3 \end{aligned} \tag{4}$$

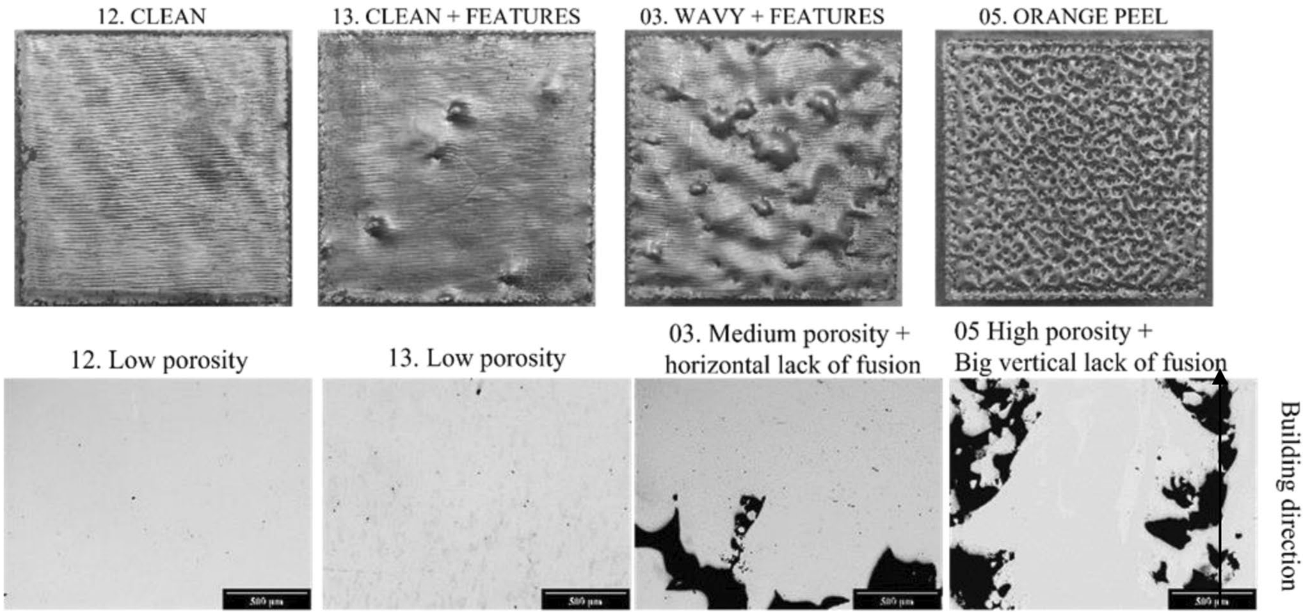

Fig. 4 Top row: qualitative inspection of top surface topography image by an optical camera at low magnification and bottom row: internal porosity obtained by OM DMI Leica. Numbers indicate the specimen codes

which has an R^2_{adj} of 0.91, whose residual normality could not be rejected with a risk of error of 5% by the Anderson Darling test, and the included terms parameters are significant with a confidence level of 95%. Equation (4) model is adequately robust and describes the influence of the melting process parameters on the internal porosity. The process-related internal defects are generated by insufficient energy input of the electron beam [68]. Therefore, the subsequent layer or adjacent line scans are not welded together; the defects generated by this phenomenon are the so-called lack of fusion. Indeed, the *FO* and the *I* (consequently *LE*) influence the electron beam diameter [69, 70], resulting in different energy input onto the powder bed. This influence cannot be thoroughly captured solely by *LE*, even though it can yield an appropriate first approximation of the electron beam irradiation, as in Zafar et al. [76], where the parameters considered are the beam voltage *V* and the beam current *I*. Conversely, a more complex combination of several parameters and the combination of the material physical properties defines the final geometry and dimension of the melt pool. The final density results from the overlap between subsequent line scan in the XY plane and the melt of different layers XZ-plane. Therefore, the width of the melt pool has to be greater than the *LO*, and the melt pool depth has to be much greater than the layer thickness.

3.3 Internal porosity and surface topography correlation

Once established and quantified, the dependence of quality variables and process parameters for the material-process pair must address the correlation between internal defectivity and surface quality.

Correlation analysis according to Sect. 2.5 is performed. According to the results obtained in Sects. 3.1 and 3.2, only *SRC*, field parameters of the waviness surfaces (S_a, S_q, and S_{dq}), and feature parameters of the SL-Surface (V_g, V_p, $A_{\%g}$ and $A_{\%p}$) are addressed, and specimens characterized by a bimodal porosity distribution are excluded from the analysis. The first choice enables the applicability of the forthcoming model and results in non-optimal process conditions, and the second is constrained by the statistical hypothesis supporting GLM. It is worth remarking that considering the discussion provided in Sect. 2.2 and the experimental methodology described in Sect. 2.1, non-optimal process parameters might hinder the evaluation of *actual* SL-Surface. Therefore, related areal field parameters are not considered.

Figure 6 shows the scatter plot of the natural logarithm of the porosity as a function of the considered topographical parameters. The logarithmic transformation is shown to ease the suggestion of the relationship to be modelled via regression. Robust regression exploiting the LAR method was performed to relieve the effect of high data dispersion [71]. Although a qualitative trend might be seen for some parameters, only the models

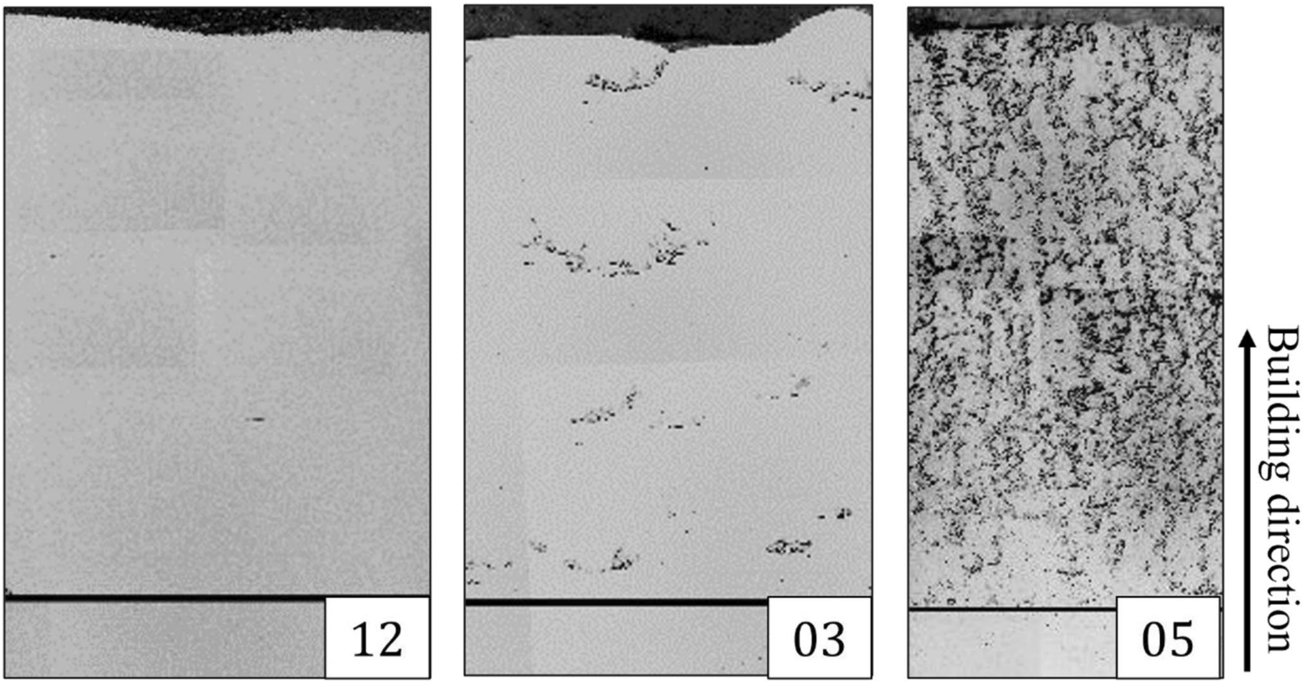

Fig. 5 Stitched images of the cross-section of the specimens: 05—high porosity level and significant vertical lack of fusion, 03—medium porosity level and horizontal lack of fusion, and 12—low porosity level

between porosity and $A_{\%p}$ and S_{dq} (in Eq. 5 and 6) were statistically significant with an R^2_{adj} of 0.95 and 0.91, respectively.

$$ln(p) = -4.637 + 0.1619 \bullet A_{\%p} - 8.9 \times 10^{-4} \bullet {A_{\%p}}^2 \quad (5)$$

$$ln(p) = -6.998 + 63.11 \bullet S_{dq} - 98.26 \bullet {S_{dq}}^2 \quad (6)$$

According to ANOVA, significant model parameters showed a p-value smaller than 5%. Residuals presented a hyper-normal distribution, suggesting a possible overfit due to the robust algorithm. Other surface topography parameters resulted in R^2_{adj} smaller than 60% (for example 30% in the case of S_a and S_q, 60% in the case of V_p). The result suggests that porosity, which has to be traced back to process parameters that influence a broad set of surface topography parameters, mainly affects the areal extension of surface pores and the spatial variability of the surface heights. This is due to the layer-wise nature of the process. Porosity in inner layers induces depression that propagates into waviness that could degenerate into topographical pores at the top surface. Indeed, large and vertical internal lack of fusions are more reasonably expected to generate an orange peel surface, while random and horizontal lack of fusion produces wavy surfaces, with the possible presence of features. Finally, no internal porosity or very low porosity populated by only spherical pores are observed in the specimen with a clean surface.

3.4 Information-rich prediction model

Results are shown in Sect. 3 allowed demonstrating a correlation between (i) internal porosity and process parameters, (ii) surface topography and process parameters, and (iii) internal porosity and surface topography, as detailed in Fig. 7.

This information can now be merged within an information-rich prediction model of the porosity. The model relies upon redundancies created by the surface topography quality inspection and characterization to improve the robustness and informativeness of the porosity modelling.

The methodology presented in Sect. 2.5 is applied, and it results in the following model:

$$\begin{aligned} ln(p) = & -65.97 + 0.26 \bullet FO + 127.81 \bullet LO + 0.92 \bullet I + 0.51 \bullet SF + 22.90 \bullet AE + \\ & +37.02 \bullet S_{dq} - 0.02 \bullet A_{\%p} + 2.33 \bullet LO \bullet SF - 0.16 \bullet FO \bullet AE - 0.20 \bullet I \bullet AE + \\ & -4.72 - 94.94 \bullet AE^2 - 94.94 \bullet {S_{dq}}^2 - 2.51 \times 10^{-4} \bullet {A_{\%p}}^2 + 0.43 \bullet AE^3 \end{aligned} \quad (7)$$

The model estimated parameters are statistically significant with a risk of error of 5% and yield residuals whose normality cannot be disproved at a confidence level of 95% by the Anderson–Darling test (Fig. 8(a) shows the NPP of the residuals). The model is associated with an R^2_{adj} of 0.95 and presents an RMSE of 0.7206, i.e. of 2% on the porosity. These results show the effectiveness in increasing the representativeness of the model when additional information from ND in situ quality controls are available. The R^2_{adj} comparison with the model only including the process parameters as predictors (see Sect. 3.2) shows 4% and 56% relative improvement to the maximum possible achievable. Model validation shows (Appendix) satisfactory results, as it can be appreciated in Fig. 8(b), where only one experimental point is systematically different from the prediction. This is compliant with risk of error of I and II type inherent in quality inspection procedures [72, 73]. Specifically, in the case at hand, a dense component is predicted, when in reality is porous, identifying a type II error.

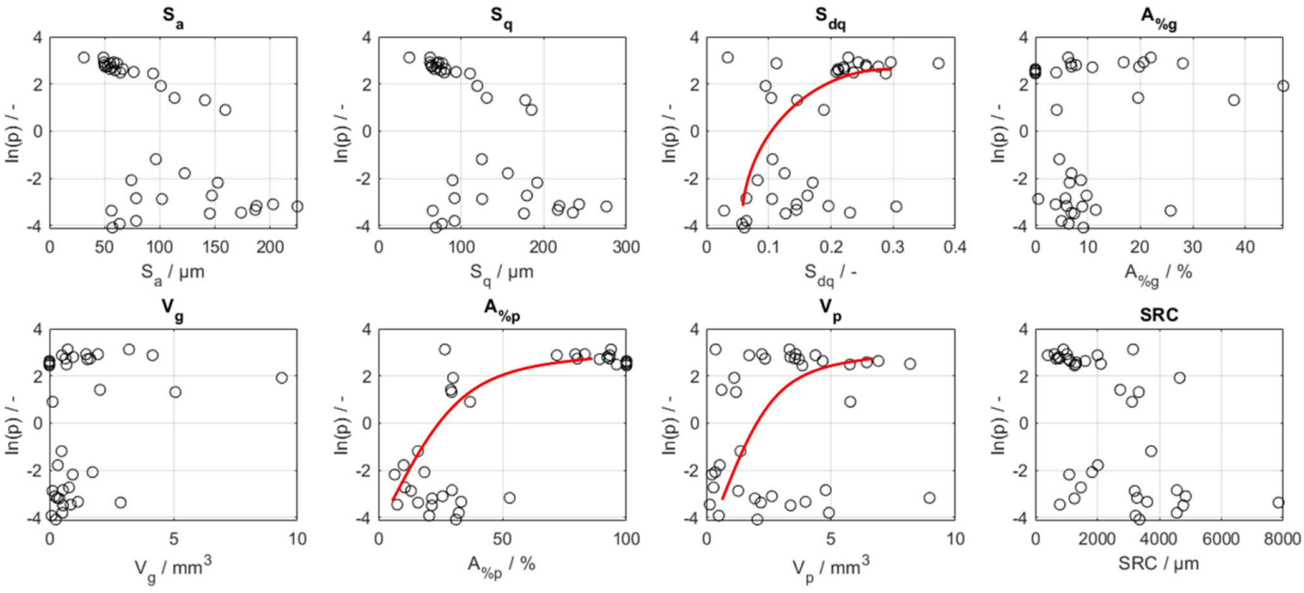

Fig. 6 Natural logarithm of the porosity as a function of field parameters of waviness surface and feature parameters of SL-Surface. Notice the qualitative trend correlating with S_{dq}, $A_{\%p}$, and V_p. Regression analysis is only evidence of correlation with the first two parameters

4 Conclusions

In this work, a new model is developed to estimate the porosity content of the parts starting from the topological investigation of the as-built samples. In fact, in this research, 52 specimens of AISI H13 tool steel samples were produced by the EB-PBF process, following an unbalanced DoE. As a result, an information-rich prediction model of the internal porosity based on the input process parameters (*I*, *SF*, *t*, *LO*, *AE*, and *LE*) and surface topographical parameters (S_{dq} and $A_{\%p}$) is presented. The results showed a robust correlation between the surface topography features and the input process parameters. Furthermore, the robust correlation of internal defectivity meant as porosity and the input process parameters were shown and related to surface topography. The correlation between internal porosity and surface parameters was only qualitatively supposed in previous literature. This work first substantiates the correlation with statistical analysis. In particular, internal porosity propagates to affect outermost surface of the material in terms of the areal extension of surface pores ($A_{\%p}$) and variability of the topography height gradient (S_{dq}). This model's development is helpful for the initial optimization of process parameters while assessing the feasibility of new materials or during quality control of the produced components. The correlation analyses established a robust information-rich prediction model of the internal porosity based on in situ surface topography characterization, and process parameters have been established. The presented methodology can help speed up the characterization step and the process optimization.

Moreover, it can aid the manufacturing process design and quality control to optimize the usage of resources towards zero-defect manufacturing by reducing scraps, and waste originating from destructive quality controls and reworks. Future development of this work will include deploying and testing the developed information-rich prediction model in relevant production environments. Potential spin off of the methodology developed is its application to real-time control of the process. Future work will also focus on the probability of defects generation basing on the proposed information-rich prediction model.

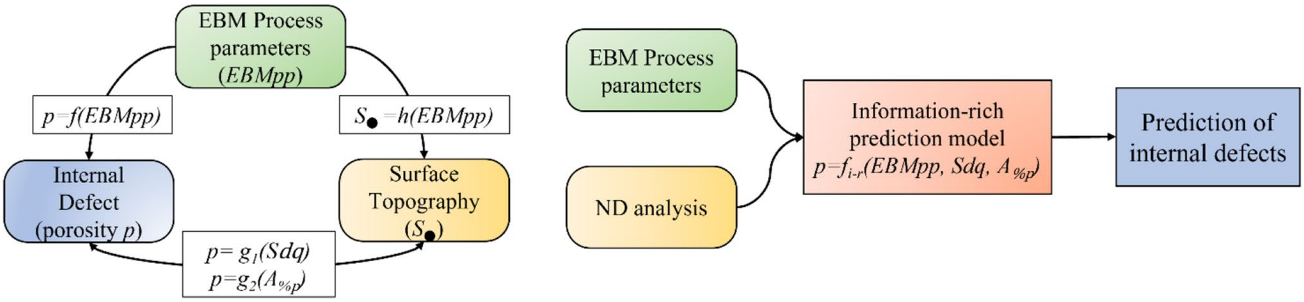

Fig. 7 Information-rich prediction model of internal porosity exploiting topographical characterization as redundancies

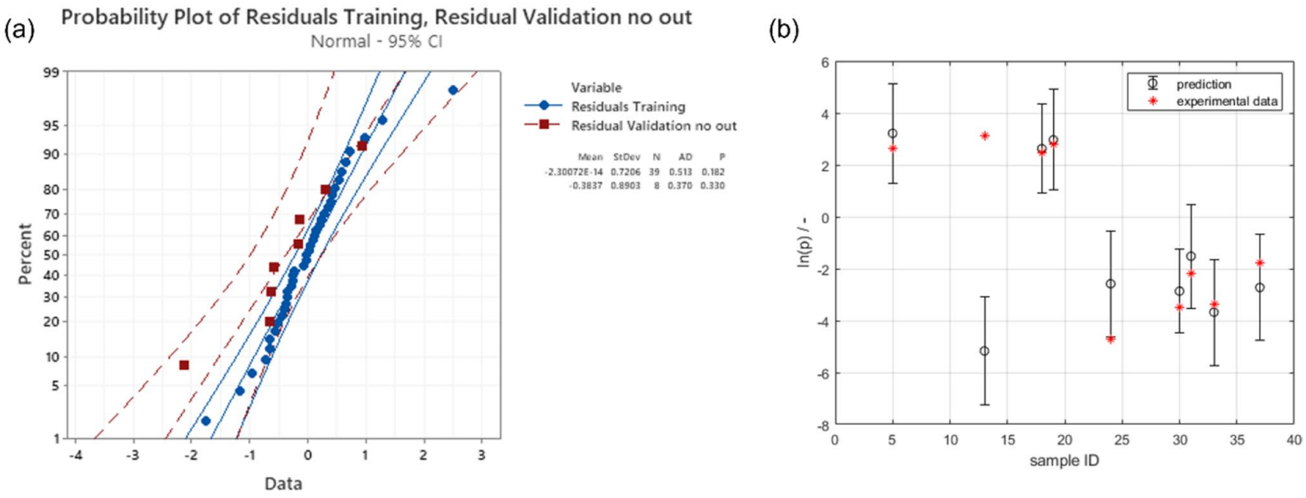

Fig. 8 Prediction training and validation results. **a** NPP of the residuals of the Information-rich prediction model (blue) and of the validation residuals (red). No systematic deviation from normal distribution can be seen with a risk of error of 5%. **b** Validation results: notice how the experimental data (red) fall inside predicted values prediction interval (evaluated at 95% confidence interval)

Appendix

Tables 6 and 7

Table 6 List of combination of process parameters, the condition with * indicate the presence of one or more repetition

Condition	I/mA	v/mm/s	F.O./mA	L.O./mm	t/mm
1	8	1333	15	0.20	0.05
2	8	533	25	0.20	0.05
3*	8	800	25	0.20	0.05
4	8	1200	25	0.20	0.05
5*	8	1600	25	0.20	0.05
6	8	2000	25	0.20	0.05
7*	8	2400	25	0.20	0.05
8	8	3200	25	0.20	0.05
9	8	800	30	0.20	0.05
10	8	1200	30	0.20	0.05
11	8	1600	30	0.20	0.05
12	8	400	35	0.20	0.05
13*	8	533	35	0.20	0.05
14	8	600	35	0.20	0.05
15*	8	800	35	0.20	0.05
16	8	1000	35	0.20	0.05
17	8	1067	35	0.20	0.05
18*	8	1200	35	0.20	0.05
19*	8	1600	35	0.20	0.05
20	8	560	35	0.20	0.05
21	8	400	35	0.25	0.05
22	8	467	35	0.25	0.05
23	8	533	35	0.25	0.05
24*	8	373	35	0.30	0.05
25	8	400	35	0.30	0.05
26	8	520	35	0.30	0.05
27*	15	1000	35	0.20	0.09
28	15	700	35	0.25	0.09
29	15	750	35	0.25	0.09
30**	15	875	35	0.25	0.09
31**	15	1000	35	0.25	0.09
32	15	700	35	0.30	0.09
33*	15	875	35	0.30	0.09
34	15	1000	35	0.30	0.09
35	15	900	35	0.25	0.09
36	15	1050	35	0.25	0.09
37	15	1100	35	0.25	0.09
38	15	900	35	0.30	0.09

Table 7 Validation data set. Results of measurements of topography and porosity. Sample condition refers to Table A 1

Condition	S_a/µm	S_q/µm	S_{dq}/-	V_p/mm3	$A_{\%p}$	V_g/mm3	$A_{\%g}$	SRC/µm	ln(p)/-	p/%
5	54.74	67.9	0.222	4.67	100%	0	0	1120	2.63	13.9%
13	31.24	37.43	0.034	0.37	26.79%	3.21	21.98%	3151	3.12	22.64%
18	64.24	79.86	0.236	5.76	96.01	0.69	3.99%	1301	2.48	12.0%
19	49.71	63.7	0.256	3.37	92.25%	0.96	7.75%	759.7	2.80	16.4%
24	17.75	24.7	0.075	0	0%	0.01	0.56%	221	-4.71	0.01%
27	122.4	156.3	0.126	0.54	10.17%	0.34	6.88%	2018	-1.79	0.17%
30	145.1	176.1	0.127	3.38	21.54%	0.55	7.43%	4772	-3.49	0.03%
31	152.3	192.1	0.171	0.22	6.56%	0.94	6.53	1095	-2.18	0.11%
33	56.2	65.62	0.029	2.19	16%	2.87	25.76	7846	-3.37	0.03%

Supplementary Information The online version contains supplementary material available at https://doi.org/10.1007/s00170-023-11153-2.

Acknowledgements The authors would like to acknowledge the Integrated Additive Manufacturing centre at Politecnico di Torino (IAM@polito) where the specimens were built.

Funding Open access funding provided by Politecnico di Torino within the CRUI-CARE Agreement. This work has been partially supported by "Ministero dell'Istruzione, dell'Università e della Ricerca." Award "TESUN-83486178370409 finanziamento dipartimenti di eccellenza CAP. 1694 TIT. 232 ART. 6."

Data availability Summary data are available in the Annex. Other data might be available upon request to the corresponding author in not subjected to study relevant to on-going studies.

Declarations

Ethics approval Not applicable.

Consent to participate Not applicable.

Consent for publication Not applicable.

Competing interests The authors declare no competing interests.

References

1. Murr LE, Gaytan SM (2014) Electron beam melting. Elsevier. https://doi.org/10.1016/B978-0-08-096532-1.01004-9
2. Biamino S, Penna A, Ackelid U, Sabbadini S, Tassa O, Fino P, Pavese M, Gennaro P, Badini C (2011) Electron beam melting of Ti-48Al-2Cr-2Nb alloy: microstructure and mechanical properties investigation. Intermetallics 19:776–781. https://doi.org/10.1016/j.intermet.2010.11.017
3. Murr LE, Martinez E, Gaytan SM, Ramirez DA, MacHado BI, Shindo PW, Martinez JL, Medina F, Wooten J, Ciscel D, Ackelid U, Wicker RB (2011) Microstructural architecture, microstructures, and mechanical properties for a nickel-base superalloy fabricated by electron beam melting. Metall Mater Trans A Phys Metall Mater Sci 42:3491–3508. https://doi.org/10.1007/s11661-011-0748-2
4. Ellis EAI, Sprayberry MA, Ledford C, Hankwitz JP, Kirka MM, Rock CD, Horn TJ, Katoh Y, Dehoff RR (2021) Processing of tungsten through electron beam melting. J Nucl Mater 555:153041. https://doi.org/10.1016/j.jnucmat.2021.153041
5. Cormier D, Harrysson O, West H (2004) Characterization of H13 steel produced via electron beam melting. Rapid Prototyp J 10:35–41. https://doi.org/10.1108/13552540410512516
6. Murr LE, Gaytan SM, Ramirez DA, Martinez E, Hernandez J, Amato KN, Shindo PW, Medina FR, Wicker RB (2012) Metal fabrication by additive manufacturing using laser and electron beam melting technologies. J Mater Sci Technol 28:1–14. https://doi.org/10.1016/S1005-0302(12)60016-4
7. Körner C (2016) Additive manufacturing of metallic components by selective electron beam melting - a review. Int Mater Rev 61:361–377. https://doi.org/10.1080/09506608.2016.1176289
8. Sochalski-Kolbus LM, Payzant EA, Cornwell PA, Watkins TR, Babu SS, Dehoff RR, Lorenz M, Ovchinnikova O, Duty C (2015) Comparison of residual stresses in Inconel 718 Simple parts made by electron beam melting and direct laser metal sintering. Metall Mater Trans A 46:1419–1432. https://doi.org/10.1007/s11661-014-2722-2
9. Galati M, Rizza G, Salmi A, Biamino S, Ghibaudo C, Fino P, Iuliano L (2021) Residual stress investigation on Ti-48Al-2Cr-2Nb samples produced by electron beam melting process. Procedia CIRP 99:336–341. https://doi.org/10.1016/j.procir.2021.03.049
10. Li N, Huang S, Zhang G, Qin R, Liu W, Xiong H, Shi G, Blackburn J (2019) Progress in additive manufacturing on new materials: a review. J Mater Sci Technol 35:242–269. https://doi.org/10.1016/j.jmst.2018.09.002
11. Fernandez-Zelaia P, Ledford C, Ellis EAI, Campbell Q, Rossy AM, Leonard DN, Kirka MM (2021) Crystallographic texture evolution in electron beam melting additive manufacturing of pure Molybdenum. Mater Des 207:109809. https://doi.org/10.1016/j.matdes.2021.109809
12. Murr LE (2018) A metallographic review of 3D printing/additive manufacturing of metal and alloy products and components. Metallogr Microstruct Anal 7:103–132. https://doi.org/10.1007/s13632-018-0433-6
13. Ren XP, Li HQ, Guo H, Shen FL, Qin CX, Zhao ET, Fang XY (2021) A comparative study on mechanical properties of

Ti–6Al–4V alloy processed by additive manufacturing vs. traditional processing. Mater Sci Eng A 817. https://doi.org/10.1016/j.msea.2021.141384

14. Rannar LE, Glad A, Gustafson CG (2007) Efficient cooling with tool inserts manufactured by electron beam melting. Rapid Prototyp J 13:128–135. https://doi.org/10.1108/13552540710750870
15. Gibbons GJ, Hansell RG (2005) Direct tool steel injection mould inserts through the Arcam EBM free-form fabrication process. Assem Autom 25:300–305. https://doi.org/10.1108/01445150510626433
16. Materials T, Company I (1993)- ASM HANDBOOK
17. Ghibaudo C, Saboori A, Marchese G, Gobber F, Biamino S, Ugues D (2021) Preliminary processability evaluation of H13 steel by electron beam melting, in: Euro PM 2021 Congr. Exhib : Accepted for publication
18. Kahlert M, Brenne F, Vollmer M, Niendorf T (2021) Influence of microstructure and defects on mechanical properties of AISI H13 manufactured by electron beam powder bed fusion. J Mater Eng Perform 30:6895–6904. https://doi.org/10.1007/s11665-021-06059-7
19. Nardwana P, Lee Y (2020) Influence of scan strategy on porosity and microstructure of Ti-6Al-4V fabricated by electron beam powder bed fusion, mater. today commun. https://www.osti.gov/pages/servlets/purl/1606739
20. Wang P, Tan X, He C, Nai MLS, Huang R, Tor SB, Wei J (2018) Scanning optical microscopy for porosity quantification of additively manufactured components. Addit Manuf 21:350–358. https://doi.org/10.1016/j.addma.2018.03.019
21. Mohammad A, Al-Ahmari AM, AlFaify A, Mohammed MK (2017) Effect of melt parameters on density and surface roughness in electron beam melting of gamma titanium aluminide alloy. Rapid Prototyp J 23:474–485. https://doi.org/10.1108/RPJ-12-2014-0187
22. Slotwinski JA, Garboczi EJ, Hebenstreit KM (2014) Porosity measurements and analysis for metal additive manufacturing process control. J Res Natl Inst Stand Technol 119:494. https://doi.org/10.6028/jres.119.019
23. Spierings AB, Schneider M, Eggenberger R (2011) Comparison of density measurement techniques for additive manufactured metallic parts. Rapid Prototyp J 17:380–386. https://doi.org/10.1108/13552541111156504
24. Hermanek P, Zanini F, Carmignato S (2019) Traceable porosity measurements in industrial components using X-ray computed tomography.J Manuf Sci Eng Trans ASME. 141. https://doi.org/10.1115/1.4043192
25. Cao D, Malakooti S, Kulkarni VN, Ren Y, Liu Y, Nie X, Qian D, Griffith DT, Lu H (2022) The effect of resin uptake on the flexural properties of compression molded sandwich composites. Wind Energy 25:71–93. https://doi.org/10.1002/we.2661
26. Elambasseril J, Lu SL, Ning YP, Liu N, Wang J, Brandt M, Tang HP, Qian M (2019) 3D characterization of defects in deep-powder-bed manufactured Ti–6Al–4V and their influence on tensile properties. Mater Sci Eng A 761:138031. https://doi.org/10.1016/j.msea.2019.138031
27. Kim FH, Pintar AL, Moylan SP, Garboczi EJ (2019) The influence of X-ray computed tomography acquisition parameters on image quality and probability of detection of additive manufacturing defects 141 1–11https://doi.org/10.1115/1.4044515
28. Grasso M, Remani A, Dickins A, Colosimo BM, Leach RK (2021) In-situ measurement and monitoring methods for metal powder bed fusion – an updated review. Meas Sci Technol 32:112001
29 Grasso M, Colosimo BM (2017) Process defects and in situ monitoring methods in metal powder bed fusion: a review. Meas Sci Technol 28:aa5c4f. https://doi.org/10.1088/1361-6501/aa5c4f
30. Franciosa P, Sokolov M, Sinha S, Sun T, Ceglarek D (2020) Deep learning enhanced digital twin for Closed-Loop In-Process quality improvement. CIRP Ann 69:369–372. https://doi.org/10.1016/j.cirp.2020.04.110
31. Gaikwad A, Yavari R, Montazeri M, Cole K, Bian L, Rao P (2020) Toward the digital twin of additive manufacturing: integrating thermal simulations, sensing, and analytics to detect process faults. IISE Trans 52:1204–1217. https://doi.org/10.1080/24725854.2019.1701753
32. Caiazzo B, Di M, Murino T, Petrillo A, Piccirillo G, Santini S (2021) state-of-the-art methods and open challenges. Comput Ind 134:103548. https://doi.org/10.1016/j.compind.2021.103548
33. Tao F, Zhang H, Liu A, Nee AYC (2019) Digital twin in industry: state-of-the-art. IEEE Trans Ind Informatics 15:2405–2415. https://doi.org/10.1109/TII.2018.2873186
34. Kurzynowski T, Madeja M, Dziedzic R, Kobiela K (2019) The effect of EBM process parameters on porosity and microstructure of Ti-5Al-5Mo-5V-1Cr-1Fe alloy, Scanning. 2019. https://doi.org/10.1155/2019/2903920
35. Yue H, Peng H, Li R, Su Y, Zhao Y, Qi K, Chen Y (2020) Selective electron beam melting of tial alloy: metallurgical defects, tensile property, and determination of process window. Adv Eng Mater 22:1–9. https://doi.org/10.1002/adem.202000194
36. Townsend A, Senin N, Blunt L, Leach RK, Taylor JS (2016) Surface texture metrology for metal additive manufacturing: a review. Precis Eng 46:34–47. https://doi.org/10.1016/j.precisioneng.2016.06.001
37. Ghibaudo C, Rizza G, Marchese G, Galati M, Iuliano L, Ugues D, Biamino S (2021) A comparison of different approches to study the porosity and surfacedefects for electron beam melting, in: Euro PM 2021, Congr Exhib
38. Lou S, Jiang X, Sun W, Zeng W, Pagani L, Scott PJ (2019) Characterisation methods for powder bed fusion processed surface topography. Precis Eng 57:1–15. https://doi.org/10.1016/j.precisioneng.2018.09.007
39. Newton L, Senin N, Chatzivagiannis E, Smith B, Leach R (2020) Feature-based characterisation of Ti6Al4V electron beam powder bed fusion surfaces fabricated at different surface orientations. Addit Manuf 35:101273. https://doi.org/10.1016/j.addma.2020.101273
40. Leach RK (2011) Optical Measurement of Surface Topography. Springer, Berlin
41. Santoso T, Syam WP, Darukumalli S, Cai Y, Helmli F, Luo X, Leach R (2020) On-machine focus variation measurement for micro-scale hybrid surface texture machining. Int J Adv Manuf Technol 109:2353–2364. https://doi.org/10.1007/s00170-020-05767-z
42. Dickins A, Widjanarko T, Sims-Waterhouse D, Thompson A, Lawes S, Senin N, Leach R (2020) Multi-view fringe projection system for surface topography measurement during metal powder bed fusion. J Opt Soc Am A 37:B93. https://doi.org/10.1364/josaa.396186
43. Mostafaei A, Zhao C, He Y, Reza Ghiaasiaan S, Shi B, Shao S, Shamsaei N, Wu Z, Kouraytem N, Sun T, Pauza J, Gordon JV, Webler B, Parab ND, Asherloo M, Guo Q, Chen L, Rollett AD (2022) Defects and anomalies in powder bed fusion metal additive manufacturing. Curr Opin Solid State Mater Sci 26:100974. https://doi.org/10.1016/j.cossms.2021.100974
44. Zhang Y, Wu L, Guo X, Kane S, Deng Y, Jung YG, Lee JH, Zhang J (2018) Additive manufacturing of metallic materials: a review. J Mater Eng Perform 27:1–13. https://doi.org/10.1007/s11665-017-2747-y
45. Schwerdtfeger J, Körner C (2014) Selective electron beam melting of Ti-48Al-2Nb-2Cr: Microstructure and aluminium loss. Intermetallics 49:29–35. https://doi.org/10.1016/j.intermet.2014.01.004
46. Prisco U, Astarita A, El Hassanin A, Franchitti S (2019) Influence of processing parameters on microstructure and roughness of electron beam melted Ti-6Al-4V titanium alloy. Mater Manuf

Process 34:1753–1760. https://doi.org/10.1080/10426914.2019.1683576

47. Guo C, Ge W, Lin F (2015) Effects of scanning parameters on material deposition during Electron Beam Selective Melting of Ti-6Al-4V powder. J Mater Process Technol 217:148–157. https://doi.org/10.1016/j.jmatprotec.2014.11.010
48. Chiba A, Daino Y, Aoyagi K, Yamanaka K (2021) Smoke suppression in electron beam melting of inconel 718 alloy powder based on insulator–metal transition of surface oxide film by mechanical stimulation, Materials (Basel) 14. https://doi.org/10.3390/ma14164662
49. Aversa A, Saboori A, Marchese G, Iuliano L, Lombardi M, Fino P (2021) Recent progress in beam-based metal additive manufacturing from a materials perspective: a review of patents. J Mater Eng Perform. https://doi.org/10.1007/s11665-021-06273-3
50. Gomez C, Su R, Thompson A, DiSciacca J, Lawes S, Leach R (2017) Optimization of surface measurement for metal additive manufacturing using coherence scanning interferometry. Opt Eng 56:111714. https://doi.org/10.1117/1.OE.56.11.111714
51. Senin N, Thompson A, Leach RK (2017) Characterisation of the topography of metal additive surface features with different measurement technologies. Meas Sci Technol 28:095003
52. Maculotti G, Genta G, Quagliotti D, Galetto M, Hansen HN (2021) Gaussian process regression-based detection and correction of disturbances in surface topography measurements. Qual Reliab Eng Int 1–18. https://doi.org/10.1002/qre.2980
53. British Standards Institution (2012) BS EN ISO 25178–2:2012. Publ, BSI Stand
54. ISO 25178–3, Geometrical product specifications (GPS) — surface texture : Areal Part 3 : Specification operators, (2012).
55. Maculotti G, Piscopo G, Marchiandi G, Atzeni E, Salmi A, Iuliano L (2022) Build orientation effect on Ti6Al4V thin-wall topography by electron beam powder bed fusion. Procedia CIRP 108C:222–227
56. Leach R (2013). Characterization of areal surface texture. https://doi.org/10.1007/978-3-642-36458-7
57. Klocke F, Arntz K, Teli M, Winands K, Wegener M, Oliari S (2017) State-of-the-art laser additive manufacturing for hot-work tool steels. Procedia CIRP 63:58–63. https://doi.org/10.1016/j.procir.2017.03.073
58. Barbato G, Barini EM, Genta G, Levi R (2011) Features and performance of some outlier detection methods. J Appl Stat 38:2133–2149. https://doi.org/10.1080/02664763.2010.545119
59. Montgomery DC (1991) Design and analysis of experiments, John Wiley & Sons
60. Murphy KP (2012) Machine Learning. A Probabilistic Perspective. https://doi.org/10.1007/978-94-011-3532-0_2
61. Klassen A, Forster VE, Juechter V, Körner C (2017) Numerical simulation of multi-component evaporation during selective electron beam melting of TiAl. J Mater Process Technol 247:280–288. https://doi.org/10.1016/j.jmatprotec.2017.04.016
62. Verna E, Biagi R, Kazasidis M, Galetto M, Bemporad E, Lupoi R (2020) Modeling of erosion response of cold-sprayed In718-Ni composite coating using full factorial design, Coatings. 10. https://doi.org/10.3390/coatings10040335
63. Franceschini F, Maisano D, Mastrogiacomo L, Pralio B (2010) Ultrasound transducers for large-scale metrology: a performance analysis for their use by the MScMS. IEEE Trans Instrum Meas 59:110–121. https://doi.org/10.1109/TIM.2009.2022106
64. Defect probability estimation for hardness-optimised parts by selective laser melting | SpringerLink, (n.d.). https://link.springer.com/article/https://doi.org/10.1007/s12541-020-00381-1 (accessed August 4, 2020).
65. Sharma MJ, Yu SJ (2015) Stepwise regression data envelopment analysis for variable reduction. Appl Math Comput 253:126–134. https://doi.org/10.1016/j.amc.2014.12.050
66. Wagner JM, Shimshak DG (2007) Stepwise selection of variables in data envelopment analysis: procedures and managerial perspectives. Eur J Oper Res 180:57–67. https://doi.org/10.1016/j.ejor.2006.02.048
67. Wang D (2014) Study of electron beam space charge effect of electrostatic focusing. Appl Mech Mater 602–605:2986–2990. https://doi.org/10.4028/www.scientific.net/AMM.602-605.2986
68. Zafar MQ, Wu C, Zhao H, Kai D, Gong Q (2021) Numerical simulation for electron beam selective melting PBF additive manufacturing of molybdenum. Int J Adv Manuf Technol 117:1575–1588. https://doi.org/10.1007/s00170-021-07671-6
69. Luo Y, Ye H, Du C, Xu H (2012) Influence of focusing thermal effect upon AZ91D magnesium alloy weld during vacuum electron beam welding. Vacuum 86:1262–1267. https://doi.org/10.1016/j.vacuum.2011.11.011
70. Wang Y, Fu P, Guan Y, Lu Z, Wei Y (2013) Research on modeling of heat source for electron beam welding fusion-solidification zone. Chinese J Aeronaut 26:217–223. https://doi.org/10.1016/j.cja.2012.12.023
71. Ruffieux C, Marazzi A, Paccaud F (1993) Exploring models for the length of stay distribution. Sozial- Und Präventivmedizin SPM 38:77–82. https://doi.org/10.1007/BF01318464
72. Galetto M, Genta G, Maculotti G, Verna E (2020) Defect probability estimation for hardness-optimised parts by selective laser melting. Int J Precis Eng Manuf 21:1739–1753. https://doi.org/10.1007/s12541-020-00381-1
73. Maculotti G, Genta G, Verna E, Bonù S, Bonù L, Cagliero R, Galetto M (2022) Minimization of defects generation in laser welding process of steel alloy for automotive application, Procedia CIRP. accepted f